Electronic Supplementary Information

An Unprecedented *c*-Oriented DDR@MWW Zeolite Hybrid Membrane: New Insights into H$_2$-Permselectivities via Six Membered-Ring Pores

Eunhee Jang,[1,†] Jeong Hyeon Lee,[2,†] Sungwon Hong,[1] Yanghwan Jeong,[1] Jin Chul Kim,[2] Dongjae Kim,[3] Hionsuck Baik,[4] Eunjoo Kim,[1] Nakwon Choi,[5,6] Jaewook Nam,[7] Sung June Cho,[8] Sang Kyu Kwak,[2,*] and Jungkyu Choi[1,*]

[1] Department of Chemical & Biological Engineering, College of Engineering, Korea University, 145 Anam-Ro, Seongbuk-Gu, Seoul 02841, Republic of Korea

[2] Department of Energy Engineering, School of Energy and Chemical Engineering, Ulsan National Institute of Science and Technology (UNIST), Ulsan 44919, Republic of Korea

[3] School of Chemical and Biological Engineering, Seoul National University, Seoul 08826, Republic of Korea

[4] Korea Basic Science Institute, Seoul Center, 145 Anam-Ro, Seongbuk-Gu, Seoul 02841, Republic of Korea

[5] Center for BioMicrosystems, Brain Science Institute, Korea Institute of Science and Technology (KIST), 5 Hwarang-ro 14-gil, Seongbuk-Gu, Seoul 02792, Republic of Korea

[6] KU-KIST Graduate School of Converging Science and Technology, Korea University, 145 Anam-Ro, Seongbuk-Gu, Seoul 02841, Republic of Korea

[7] Institute of Chemical Process, School of Chemical and Biological Engineering, Seoul National University, Seoul 08826, Republic of Korea

[8] Department of Chemical Engineering, Chonnam National University, 77 Yongbong-Ro, Buk-Gu, Gwangju 61186, Republic of Korea

[†] These two equally contributed to this work.

[*] Corresponding authors

(SKK) E-mail address: skkwak@unist.ac.kr and Phone: +82-52-217-2541

(JC) E-mail address: jungkyu_choi@korea.ac.kr, Phone: +82-2-3290-4854, and Fax: +82-2-926-6102

S1. Materials and Methods

S1.1. Synthesis of MWW type zeolite particles

First, the MCM-22 precursor (hereafter denoted MCM-22(P)) was synthesized as per a method described in literature.[1] Specifically, NaOH (98% pellet, Sigma-Aldrich) and sodium aluminate (45 wt% Na_2O and 55 wt% Al_2O_3, Sigma-Aldrich) were added to deionized (DI) water in a plastic bottle. Hexamethyleneimine (HMI, 97% Sigma-Aldrich) was subsequently added to the mixture. Fumed silica (CAB-O-SIL® M-5, Cabot Corporation) was slowly added to the above solution while stirring. The final mass composition of the synthetic mixture was 1 SiO_2: 0.1 NaOH: 0.03 $NaAlO_2$: 0.8 HMI: 13.1 H_2O. The mixture was vigorously mixed using a shaker overnight and transferred to a Teflon liner. The Teflon liner was mounted in an autoclave, which was placed in a rotating rack inside an oven preheated to 135 °C. The reaction was conducted for 11 d with rotation at 40 rpm. After the reaction, the autoclave was quenched by cooling with tap water. The resulting MCM-22(P) was recovered using five centrifugation and washing cycles. The MCM-22(P) powder was further calcined at 550 °C for 12 h at a ramp rate of 1 °C·min^{-1} under 200 mL·min^{-1} air flow, yielding MCM-22 particles.

S1.2. MCM-22 seed layer formation

MCM-22 seed layers on α-Al_2O_3 discs were acquired via the sonication-assisted deposition method described in the literature.[2] Specifically, approximately 0.05 g of calcined MCM-22 particles, 40 mL of anhydrous toluene, and an α-Al_2O_3 disc (sandwiched between cover glasses and vertically positioned with the help of a Teflon holder) were placed sequentially in a dried glass reactor. Subsequently, the glass reactor was sealed with parafilm, and sonication (UC-10P, JEIO Tech, South Korea) was conducted for approximately 20 min. After sonication was performed, the α-Al_2O_3 disc was recovered and briefly washed with fresh toluene. The resulting MCM-22 seed layer was calcined by

heating to 450 °C for 12 h at a ramp rate of 0.5 °C·min^{-1} under 200 mL·min^{-1} air flow. The MCM-22 seed layer is referred to as layer M.

S1.3. Secondary and tertiary growth for the formation of hybrid films

The MCM-22 seed layer (i.e., layer M) was further exposed to secondary hydrothermal growth. First, the synthetic sol for the synthesis of DDR zeolites was prepared based on a previous report.[3] The molar composition of the final sol was 9 1-adamantylamine (97%, Sigma-Aldrich): 150 ethylenediamine (99%, Sigma-Aldrich): 100 fumed silica (CAB-O_Sil, M5): 4000 H_2O. Second, layer M was placed in a Teflon liner with the help of a Teflon holder; the seeded surface was tilted and positioned facing downward. Third, the prepared solution was poured into the Teflon liner in a stainless steel autoclave. The autoclave was placed in a rack in an oven preheated to 160 °C and the reaction was carried out for 1, 2, or 3 d and quenching was performed via cooling with tap water. The recovered layer M was washed extensively with DI water and calcined at 550 °C for 12 h at a ramp rate of 0.5 °C·min^{-1} under 200 mL·min^{-1} air flow. The recovered α-Al_2O_3 disc is denoted as layer MD_xd, where M, D, and x indicate MCM-22 and DDR zeolites, and the hydrothermal reaction time in days (1, 2, or 3), respectively.

The calcined layer MD was inter-grown using a synthetic precursor that allows for the synthesis of ZSM-58 (DDR type zeolite). The synthetic precursor was prepared by adding the structure directing agent (SDA) of methyltropinium iodide (MTI). The details of the procedure used to prepare the synthetic precursor have been described in a previous study.[4] The hydrothermal reaction was carried out in an oven preheated at 130 °C for 5 or 10 d and completed by quenching with tap water. The resulting membranes were soaked in DI water in an effort to remove any impurities and then dried in an oven at 100 °C overnight. The resulting membranes are referred to as MDZ_xd (x = 5 or 10), where M, D, and Z represent MCM-22, DDR, and ZSM-58 zeolites, respectively, and x indicates the hydrothermal reaction time (in days) for tertiary growth.

In addition, we attempted to evaluate the structural compatibility for the heteroepitaxial growth of DDR@MWW. To achieve this, layer M was exposed to the secondary hydrothermal growth of the MFI type zeolite. The synthetic sol for the MFI zeolites was prepared following a previous report.[5] The molar composition of the synthetic sol was 40 SiO_2 (tetraethyl orthosilicate, reagent grade, Sigma-Aldrich): 9 tetrapropylammonium hydroxide (1.0 M in H_2O, Sigma-Aldrich): 9500 DI water: 160 ethanol. The resulting sol was poured into a Teflon-lined autoclave in which layer M had been positioned as mentioned above. The autoclave was placed in a preheated oven at 175 °C and the reaction was carried out for 1, 3, and 5 d. The recovered layer M was washed with DI water and, further, calcined at 550 °C for 12 h at a ramp rate of 0.5 °C·min^{-1} under 200 mL·min^{-1} air flow. For convenience, the resulting layer is referred to as layer MM_xd, where M and M denote the MCM-22 and MFI zeolites, respectively, and x indicates the hydrothermal reaction time in days (1, 3, or 5), respectively.

S1.4. Rapid thermal processing and activation of zeolite membranes

To control defect structures, rapid thermal processing (RTP), as reported in the literature,[6] was used to treat as-synthesized membranes (MDZ_5d or MDZ_10d). Specifically, an as-synthesized membrane was placed in a quartz tube under argon flow of 200 mL·min^{-1} and the preheated furnace (nominally around 1000 °C) was quickly moved toward the membrane. After 1 min, the furnace was moved away from the membrane. The membranes both receiving and not receiving RTP treatment were further calcined at 550 °C for 12 h at a ramp rate of 0.5 °C·min^{-1} under an air flow of 200 mL·min^{-1}. The RTP-treated MDZ membranes are denoted MDZ_xd_RC, where R and C in RC stand for the rapid thermal processing and the subsequent conventional slow calcination, respectively. In contrast, MDZ membranes not receiving RTP treatment are referred to as MDZ_xd_C where C represents the conventional slow calcination.

S1.5. Characterizations

The morphologies of the zeolite particles and films were investigated via scanning electron microscopy (SEM, Hitachi S-4300) images. Before the measurement process was conducted, a Pt coating was applied to the samples. The X-ray diffraction (XRD) patterns were obtained using an XRD3003 (SEIFERT) and used to confirm the zeolite crystalline phase and an out-of-plane orientation of a seed layer and a zeolite film. For the out-of-plane orientation, crystallographic preferential orientation values were acquired by analyzing the XRD patterns of the powder and membrane samples;[2] the XRD peaks corresponding to the (003) and (101) planes were considered. In addition, for the structural analysis of layer MD_2d, the XRD data were collected in reflection mode using a Rigaku Model D/MAX Ultima III (Japan) instrument with Cu K_α radiation (λ = 0.154 nm); the accelerating voltage and current values employed were 40 kV and 40 mA, respectively. The powder XRD patterns were indexed using the DICVOL06 program implemented in the FullProf program suite.[7, 8] The crystal structures of the MWW and DDR zeolite frameworks were acquired from the Database of Zeolite Structures (http://www.iza-structure.org/databases/) and used for Le Bail refinement.[9] Profile refinement of the structure model was performed using the Rietveld method in the JANA2006 package.[10] During Le Bail refinement, a pseudo-Voigt function and microscopic broadening, along with a manually interpolated background, were used to describe the peak shapes. The agreement factors shown in Fig. 2a are reasonable. The phase fraction of the DDR zeolite estimated from Le Bail refinement was ca. 95%, suggesting the pronounced presence of the DDR zeolite in layer MD_2d.

To demonstrate the heteroepitaxial growth of the DDR type zeolite on the MWW type zeolite, the fast Fourier transformation (FFT) pattern of a particle detached from layer MD_2d was acquired. To detach particles, a layer sample (i.e., layer MD_2d) was sonicated for 3 min in 10 mL of ethanol. The particles in the sonicated sol were placed on a TEM grid by dropping. The FFT pattern was generated from high-resolution transmission electron microscopy (HR-TEM, Tecnai G^2 F30ST) image of layer

MD_2d obtained using a 300-kV accelerated electron beam. The HR-TEM image was obtained along the direction perpendicular the basal plane of layer MD_2d. In addition, Digital Micrograph (Gatan, Inc.) was used to simulate the FFT patterns. In addition, a cross-sectional specimen of MDZ_10d_RC was prepared by using a Helios G4 UC dual beam-focused ion beam (DB-FIB). Before conducting FIB, a Pt layer was deposited on the surface of MDZ_10d_RC in an effort to prevent any damage by the ion beam. Then, FIB with Ga ions thinned the thickness of the cross-sectioned specimen to ~100 nm to be suitable for TEM analysis. The prepared cross-sectioned specimen was used to obtain the cross-sectional view TEM images. For this task, we used an FEI XFEG-Titan Themis[3] Double Cs & Mono. TEM. To investigate the defect structure of a zeolite membrane, fluorescence confocal optical microscopy (FCOM, ZEISS LSM-700) analysis with a solid-state laser (555 nm wavelength) was used. For the FCOM measurements, the membrane samples were dyed with a fluorescent molecule (fluorescein sodium salt, $C_{20}H_{10}Na_2O_5$, Sigma-Aldrich (Product No.: F6377)) having an approximate diameter of ca. 1 nm,[11] which is larger than that of the zeolite pores (< 1 nm) but smaller than the defect size ($\geq$ 1 nm). Thus, the fluorescent molecules can selectively access the defects, while diffusion into the zeolite pores is excluded. The membrane dyeing process was conducted using an osmosis-type dye contactor; detailed information about this process has been reported in a previous study.[12] In the dye contactor, the surface of the membrane sample was in contact with the 1 mM fluorescein sodium salt solution, whereas the opposite support side was in contact with DI water. In this study, membrane dyeing was carried out for 12, 24, and 60 h. The FCOM images, which were obtained along the membrane thickness, were used to extract the quantitative properties (tortuosity and porosity) of the defect structure in the membranes via image processing. Detailed information about the image processing method can be found elsewhere.[13]

The H_2/CO_2, CO_2/N_2 and CO_2/CH_4 separation performance tests through the MDZ membrane series were implemented using a home-made permeation cell in a Wicke-Kallenbach system. The total pressures of both the feed and permeate sides were maintained at ca. 1 atm. The feed partial pressures of equimolar binary mixtures under dry conditions were 50.5 and 50.5 kPa, respectively. Under wet

conditions, the partial pressures of the binary mixtures and H_2O vapor were 49, 49, and 3 kPa, respectively. The feed mixtures with ca. 100 mL·min⁻¹ (on the dry basis) were fed into the feed stream, and He sweep gas of ca. 100 mL·min⁻¹ was fed to the permeate side. A gas chromatography (GC; YL 6100 GC, YL Instrument) system equipped with a packed column (6 ft × 1/8" Porapak T) and thermal conductivity detector (TCD) was employed for the on-line detection of CO_2 and N_2 permeates. In addition, for the H_2/CO_2 and CO_2/CH_4 separation performance tests, a GC system (YL 6500 GC System, YL Instrument) equipped with a capillary column (30 m × 0.320 mm GS-GasPro) and a pulsed discharge ionization detector (PDD) was employed for the on-line detection of H_2 and CO_2 permeates or CO_2 and CH_4 permeates. For obtaining reliable measurements, internal standards of approximately 5 mL·min⁻¹ of CH_4 and 5 mL·min⁻¹ of H_2 were employed to measure the permeation rates of gas pairs: H_2/CO_2 (or CO_2/N_2) and CO_2/CH_4, respectively.

S2. Computational modeling

S2.1. Density functional theory calculations

To investigate the diffusion energy barriers and binding energies of gas molecules, cage-shaped cluster models of the DDR zeolite were constructed for density functional theory (DFT) calculations. To represent the (001) plane of the *c*-out-of-plane oriented DDR zeolite membrane, a 46T model was generated using a whole dtr cage ($4^35^{12}6^18^3$) and half of an adjacent dtr cage along with employing a partial optimization procedure (Fig. S17a).[14, 15] In addition, to represent the (101) plane of the (*101*)-oriented DDR zeolite membrane and investigate the interactions of gas molecules with the non-zeolitic defects, a 48T model, composed of a dtr cage and a portion of det ($4^35^66^1$) and red (5^{12}) cages to describe the 8-MR pore window and surface structure, was considered (Fig. S17b), as used in our previous study.[4] All DFT calculations were conducted using the Dmol³ program.[16, 17] Specifically, we employed the Perdew-Burke-Ernzerhof (PBE) exchange-correlation function[18] with the DNP 4.4 basis set. The convergence criteria for energy, force, and displacement were set to 1×10^{-5} Ha, 0.002 Ha·Å⁻¹, and 0.005

Å, respectively. To consider the van der Waals effects, the Tkatchenko-Scheffler scheme[19] was adopted. The potential energy barrier of a gas molecule passing through the 6 MR pores was calculated by placing the C atom in CO_2 and one of two H atoms in H_2 at the center of mass of the 6-MR pore in the 46T model and by moving the molecule in the direction perpendicular to the 6-MR pore (Fig. 5a). In addition, the binding energy ($\Delta B.E.$) of a gas molecule to the grain boundary of the DDR membrane (i.e., 48T model) was calculated by using the following equation,

$$\Delta B.E. = E_{gas+zeo-48T} - (E_{gas} + E_{zeo-48T}),$$

where $E_{gas+zeo-48T}$, E_{gas}, and $E_{zeo-48T}$ are the total energies of the gas-adsorbed 48T model, an isolated gas molecule, and the 48T model, respectively.

S2.2. Nonequilibrium molecular dynamics (NEMD)

To predict the permeability of the gas molecules through the DDR membrane, nonequilibrium molecular dynamics (NEMD) simulations implemented by the LAMMPS package[20] were applied to a DDR slab model. We constructed two slab models, where the z-axis was set to be perpendicular to either the (001) plane (Fig. S17c) or the (101) plane (Fig. S17d) of the DDR zeolite. In both models, there was a 5-nm thin membrane layer along with a 50.0-nm-long region (on the feed side) and a 20.0-nm-long region (on the permeation side). In addition, to examine the effect of defects on the permeabilities, we removed a part (reflected by an empty gap) of the slab model to describe a defect, while considering the cage structure exposed to the defect structure. Accordingly, this resulted in a planar defect structure of a width d; this planar structure was employed in an effort to describe cracks present in MDZ_10d. In this study, we considered four cases of defects in each slab model (d = 0.6, 0.8, 1.0, and 2.0 nm). At the membrane surface and planar defect surface, silanol groups (Si-OH) were used as terminating groups. Along the z-axis of the slab model, we considered a non-periodic condition and placed impermeable walls in the simulation box so that gas molecules could not move directly from the feed region to the permeation region without passing though the zeolite membrane layer. The molecular models and force field

parameters of CO_2 and H_2 were employed as per the EPM2 model of Harris and Yung[21] and the monoatomic model developed by Kumar et al.[22], respectively. For the atomic charges and van der Waals parameters of the DDR zeolite, we employed CLAYFF.[23]

The NEMD simulations were conducted for 6 ns at four different inlet pressure conditions (CO_2:H_2 = (1) 50 kPa:50 kPa, (2) 100 kPa:100 kPa, (3) 250 kPa:250 kPa, and (4) 500 kPa:500 kPa) and two temperature conditions (T = 30 and 200 °C). The simulations were carried out by maintaining the total number of gas molecules to ensure a constant pressure difference between the feed and permeation regions. To reduce the perturbing effects when adding or removing molecules, we assigned the halves of the feed and permeation regions as the inlet and outlet control regions, respectively (Fig. S17c-d). While we kept counting the gas molecules (related to the permeability) that had passed through the membrane model, at every 100 ps, we counted the number of gas molecules in the control regions of both the feed and permeation regions and added or removed CO_2 and H_2 gas molecules to the feed part or from the permeation part, respectively, to maintain an initial number (i.e., partial pressure) of each component. The initial number of gas molecules in the feed region was obtained via grand canonical Monte Carlo simulation (GCMC), as shown in Table S1, whereas that of the permeation region was set to zero. We implemented the GCMC simulation using a Sorption program,[24] and employed the same molecular models and force field parameters of gas molecules employed in the NEMD simulation. GCMC simulations of 5×10^6 equilibrium and 5×10^6 production steps were performed to obtain the initial number of gas molecules at each pressure and temperature in the feed region.

S3. Supplemental discussion regarding experimental results

In addition, the water vapor in the feed increased the CO_2/N_2 SF at the expense of a reduced CO_2 permeance especially below 100 °C (Fig. S11b1-b2). In contrast, the reduced degree of the permeance was higher for CO_2 than CH_4 in the CO_2/CH_4 separation, thereby decreasing the corresponding CO_2/CH_4

SF up to approximately 50 °C under wet conditions (Fig. S11c1-c2). In particular, the trends in CO_2/N_2 and CO_2/CH_4 separations induced by water vapor were quite similar to those of the reported homogeneous DDR membrane.[4] The main difference is the aforementioned lowered CO_2 permeance in MDZ_10d_RC, apparently arising from the significant portion of preferentially *c*-out-of-plane oriented DDR zeolite. The higher CO_2/N_2 SF under wet conditions could be ascribed to the hydrophobicity of siliceous DDR zeolites in MDZ_10d_RC (see the inset of Fig. 1e),[4, 25] as supported by water contact angle measurements, which yielded a contact angle of 75° (Fig. S12). In contrast, in contact angle measurements of MDZ_10d_C, the water droplet quickly penetrated the sample and disappeared, indicating the presence of many defects in MDZ_10d_C (Fig. S12).

S4. Supplemental discussion regarding simulation results

S4.1. Permeation through the (*001*)-oriented DDR membranes

To estimate the permeability of CO_2 and H_2 through the zeolite membranes, 1-ns NEMD simulations were conducted and repeated six times. For analysis, we chose the results of the 4th, 5th, and 6th simulations to estimate the molar fluxes. The number of permeated molecules across the zeolite membrane showed a linear dependence on the feed pressure (Fig. S18). However, CO_2 could not even pass through the zeolite membrane having 0.6-nm-thick defects at low feed pressure, suggesting that the 0.6-nm-thick defect was too narrow. Further, this impermeability was observed at the highest pressure considered in this study (i.e., 500 kPa) at 200 °C. To observe the effect of pressure on the permeation rate, the slope of the linear regression line obtained from the number of permeating molecules versus pressure (equivalent to permeance) is shown in Fig. 5c. The permeability of H_2 was always higher than that of CO_2, regardless of the pressure and temperature conditions considered in this study. This trend was inconsistent with the permeation results of the *c*-oriented hybrid membrane (MDZ_10d_RC) obtained in this study (Fig. 3b). Because, in general, the zeolite membrane contained defects (here, cracks, as shown in Fig. 4c2-c4 and 4d2-d4), we also calculated the permeabilities of CO_2 and H_2 through the (*001*)-

oriented DDR membrane containing planar defects (of up to ca. 2 nm). However, the aforementioned trend in higher H_2 permeability was not changed, but the increased defect size resulted in the larger permeabilities (Figs. 5c and S18).

Considering molecular transport through microporous defects, the transport of CO_2 was likely to be more energetically favorable than that of H_2 because of the preferred adsorption of CO_2 on the presumed defect surface over H_2. Specifically, the binding energy of CO_2 on the surface of the 48T model based on the DFT calculations was -7.19 kcal·mol^{-1}, which was significantly larger than that of H_2 (-3.47 kcal·mol^{-1}) (Fig. S20). However, the corresponding MD-based permeances, which are coupled functions of diffusion and adsorption, clearly indicate the overall facilitated transport of H_2 over CO_2 across the defects (Fig. 5c), strongly showing that MD simulations are useful for predicting the intrinsic or extrinsic permeation results of zeolite membranes. Furthermore, to understand the low permeability of CO_2 in the NEMD simulations, additional DFT calculations with the 48T model were conducted (Fig. S21). At the pore mouth of an 8-MR pore, the binding energy of CO_2 (-11.86 kcal·mol^{-1}) was much larger than that near the defect surface (-7.19 kcal·mol^{-1}). Notably, the difference in binding energy (ΔE) of CO_2 and H_2 with a zeolite structure was larger at the pore mouth (i.e., 7.61 kcal·mol^{-1} at the pore mouth as in Fig. S21 vs. ΔE = 3.72 kcal·mol^{-1} near the defect surface as in Fig. S20). This implies that CO_2 could preferentially diffuse along the 8-MR pores in the DDR zeolite (i.e., from the defect side to the DDR zeolite portion (in-plane directions) instead of going through the defects (out-of-plane direction)) rather than the defects having widths of up to 2.0 nm, though the CO_2 permeances increased with increasing defect width (Figs. 5c and S18).

S4.2. Permeation through the (*101*)-oriented DDR membranes

In addition, we considered another preferred out-of-plane case in the DDR zeolite membrane. Specifically, the (*101*)-oriented DDR zeolite membrane reported in our previous study[4] was chosen,

because the corresponding experimental results are available. The permeabilities of CO_2 and H_2 molecules passing through the (*101*)-oriented DDR zeolite membrane were calculated at a variety of feed pressures, temperatures, and defect widths (Figs. 5d and S19). In general, the number of permeating gas molecules increased with increasing defect width, as for case of the (*001*)- or *c*-oriented DDR zeolite membrane (Figs. 5c and S18). As expected from Fig. S21, the CO_2 permeability at 30 °C was higher than that of H_2, seemingly because of the energetically favorable adsorption of CO_2 molecules at the pore mouth of the 8-MR pore. However, this characteristic trend, likely determined by the affinity of H_2 or CO_2 onto the DDR zeolite, was reversed at an elevated temperature of 200 °C. It appears that the elevated temperature activated the diffusion of H_2 across the 8-MR pores over CO_2. Moreover, this temperature dependency of permeation rates agreed with experimental results of the (*101*)-oriented DDR zeolite membrane.[4]
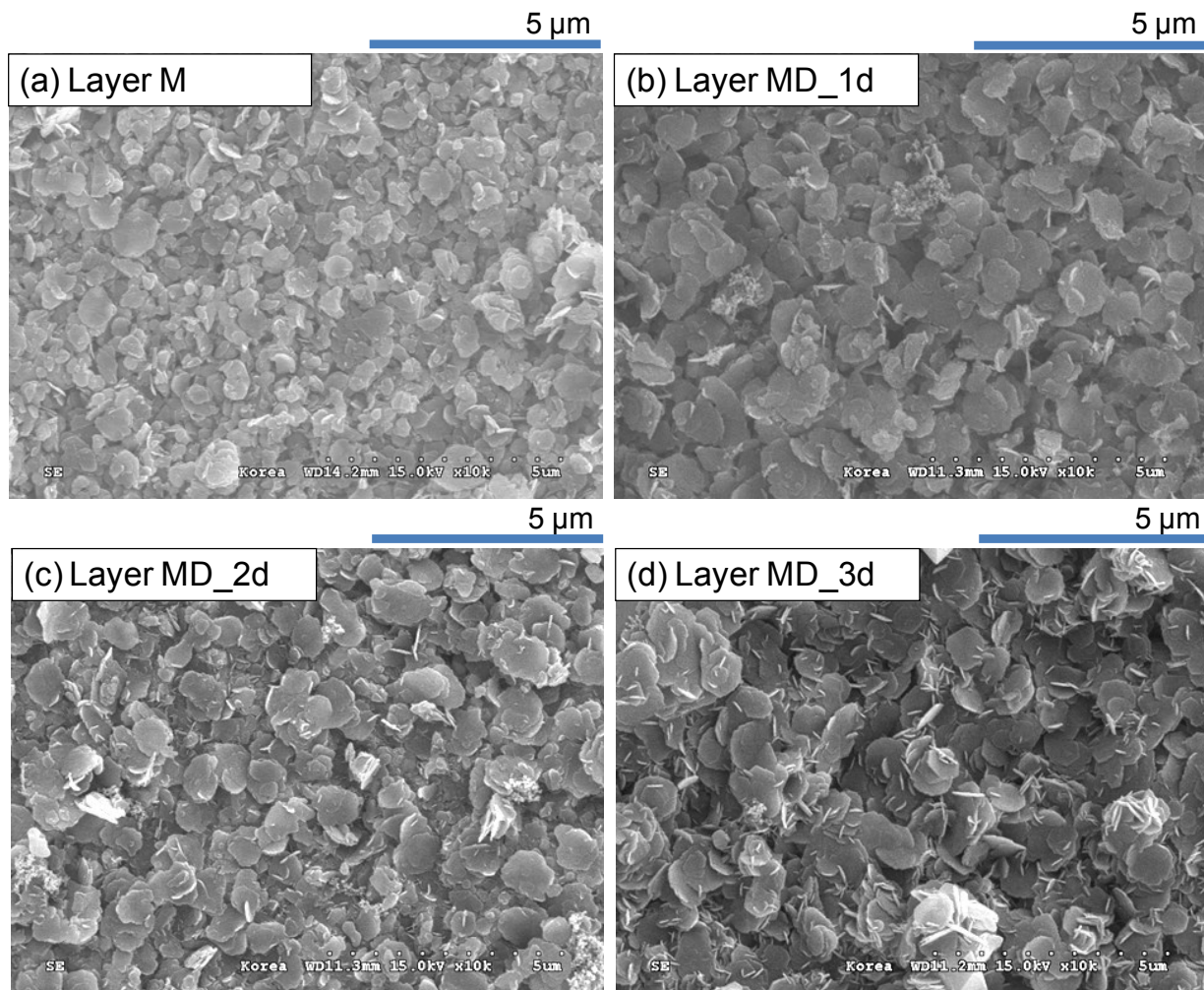
Fig. S1. Top view SEM images of layers (a) M, (b) MD_1d, (c) MD_2d, and (d) MD_3d.
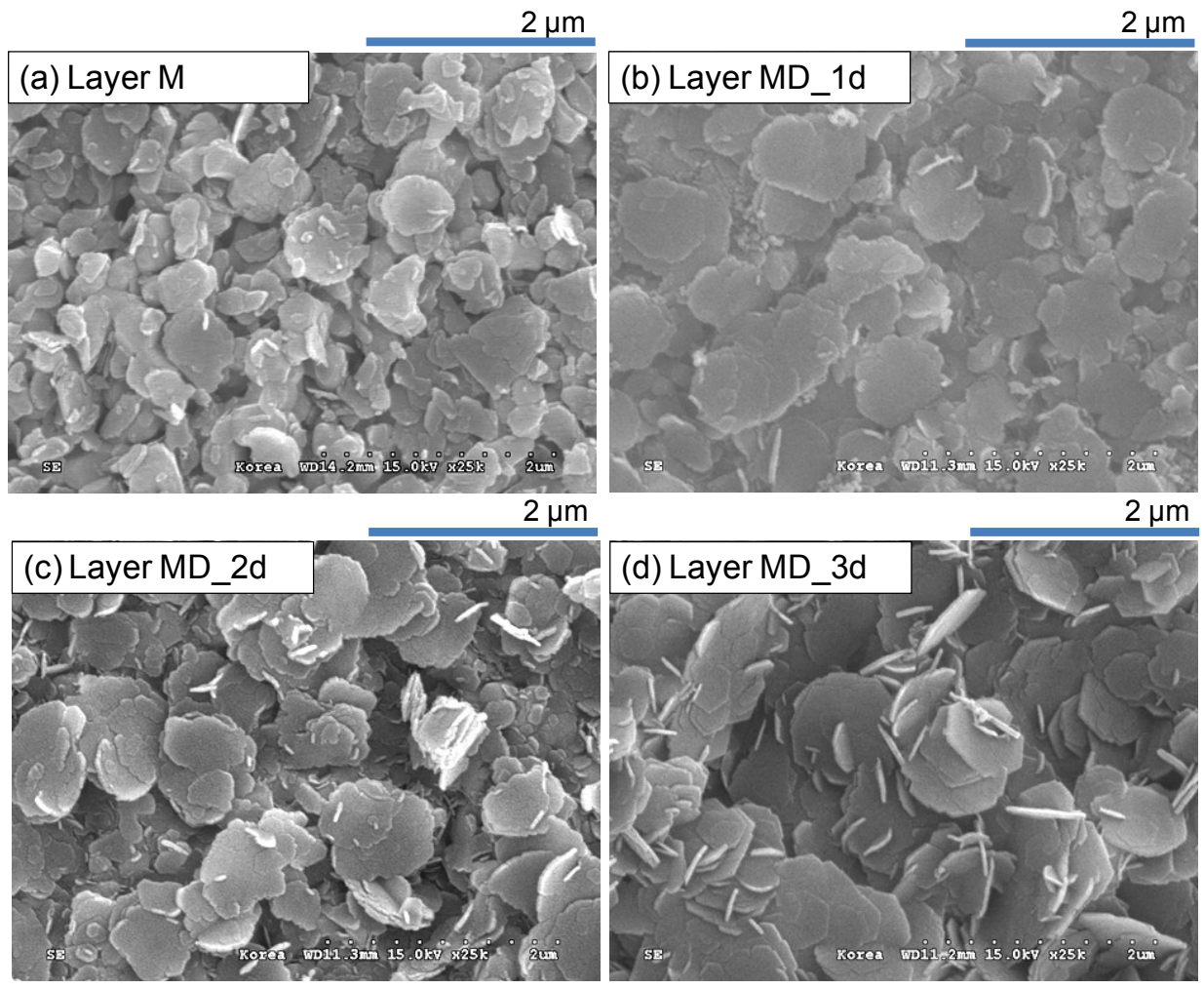
Fig. S2. Top view SEM images of layers (a) M, (b) MD_1d, (c) MD_2d, and (d) MD_3d at a higher magnification relative to those shown in Fig. S1.
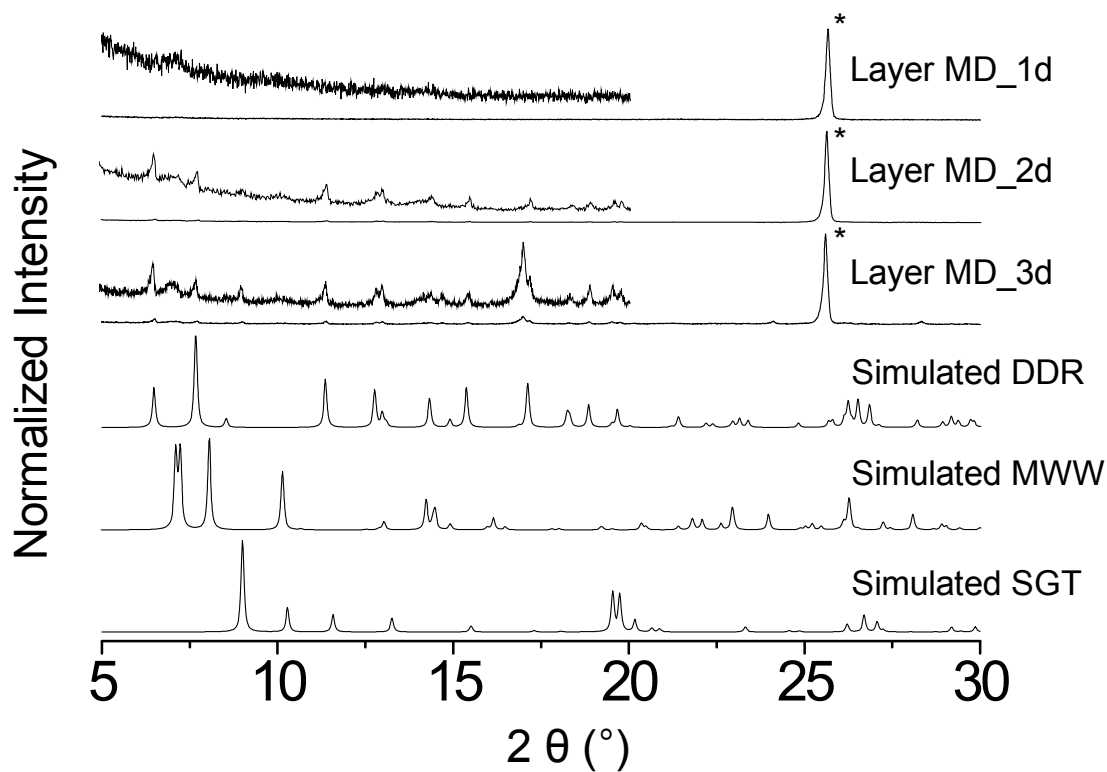
Fig. S3. XRD patterns of layers MD_1d, _2d, and _3d along with the simulated XRD patterns of all-silica DDR, MWW, and SGT type zeolites. The XRD patterns of layers MD_1d, _2d, and _3d in the 2θ range of 5-20° are magnified and displayed on the top of the original XRD patterns. The asterisks (*) represent the XRD peaks corresponding to the α-Al$_2$O$_3$ disc.
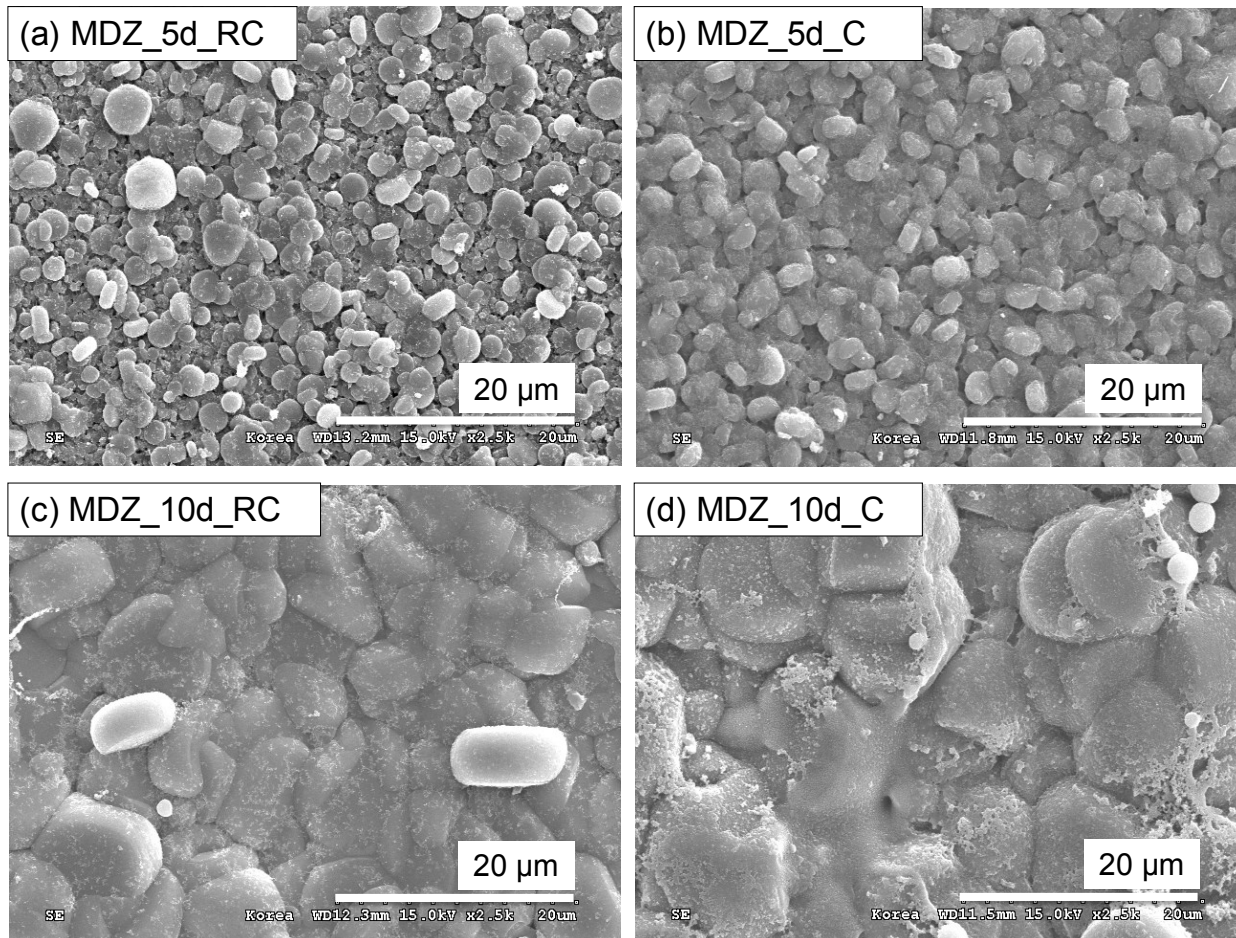
Fig. S4. SEM images of (a) MDZ_5d_RC, (b) MDZ_5d_C, (c) MDZ_10d_RC, and (d) MDZ_10d_C. The scale bars represent 20 μm.
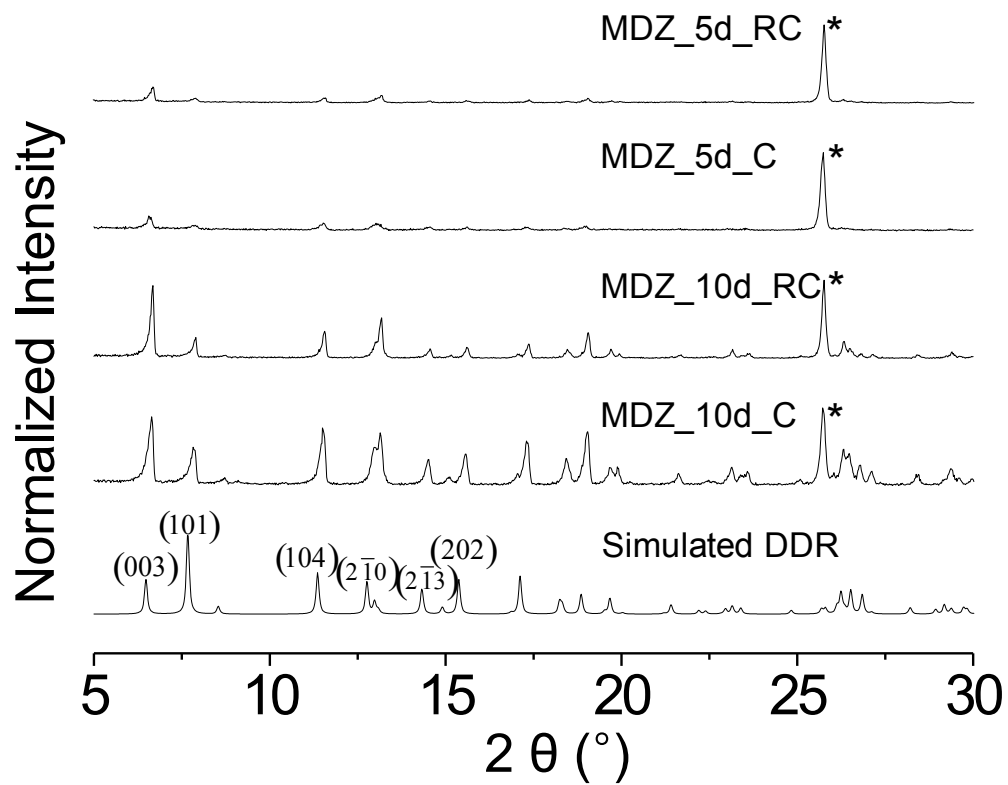
Fig. S5. XRD patterns of MDZ_5d_RC, MDZ_5d_C, MDZ_10d_RC, and MDZ_10d_C from the *1st row* to the *4th row*, respectively, along with the simulated XRD pattern of the DDR zeolite (*bottom*). The asterisk (*) represents the XRD peak arising from the α-Al_2O_3 disc.
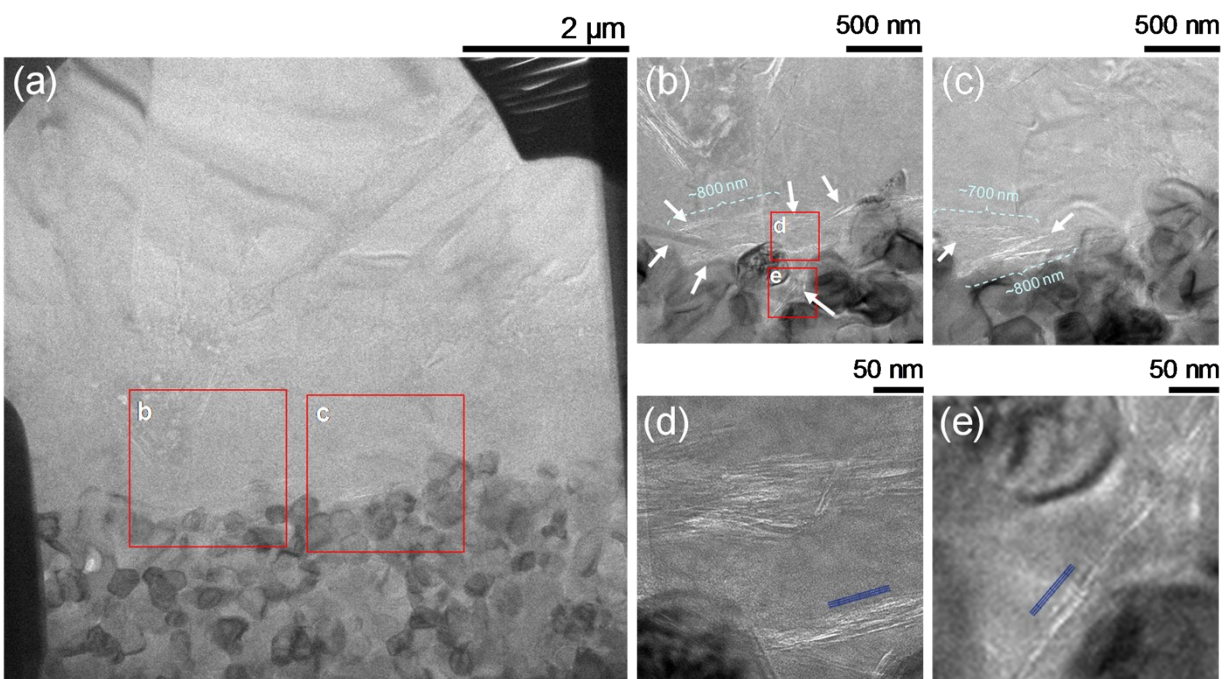
Fig. S6. (a)-(e) Cross-sectional view TEM images of MDZ_10d_RC at different magnifications; increasing in order of (a), (b)-(c), and (d)-(e). The areas marked in red squares in (a) are shown in (b) and (c), while those marked in red squares in (b) are magnified and demonstrated in (d) and (e). For convenience, in (b)-(c), some white arrows are added to indicate needle-like particles (plausibly, obtained as a result of cutting in the direction perpendicular to disc-like MCM-22 seed particles) and approximate lengths of needle-like particles (~700-800 nm; these are close to the size (~1 μm) of the disc-like MCM-22 particles shown in Figs. 1a and S2a) are given. In addition, in (d)-(e), the MCM-22 structure models projected along the *b*-axis are displayed next to the needle-like particles.
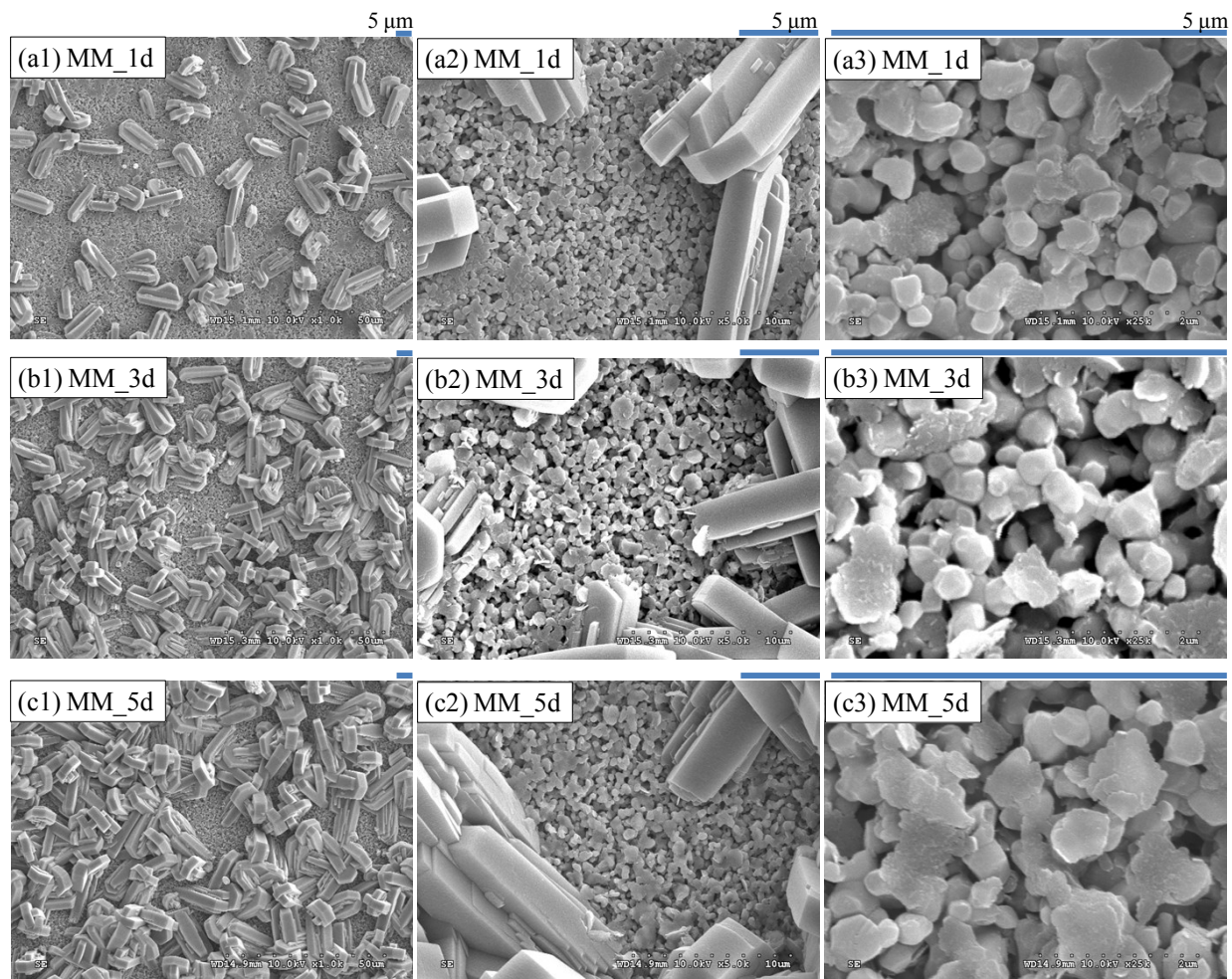
Fig. S7. SEM images of (a1)-(a3) MM_1d, (b1)-(b3) MM_3d, and (c1)-(c3) MM_5d at increasing magnifications. The blue scale bars represent 5 μm. For convenience, samples obtained after the secondary growth of layer M are referred to as MM_*x*d, where the second "M" represents the MFI type zeolite growth and *x* indicates the used time (in days) for the secondary growth of layer M.
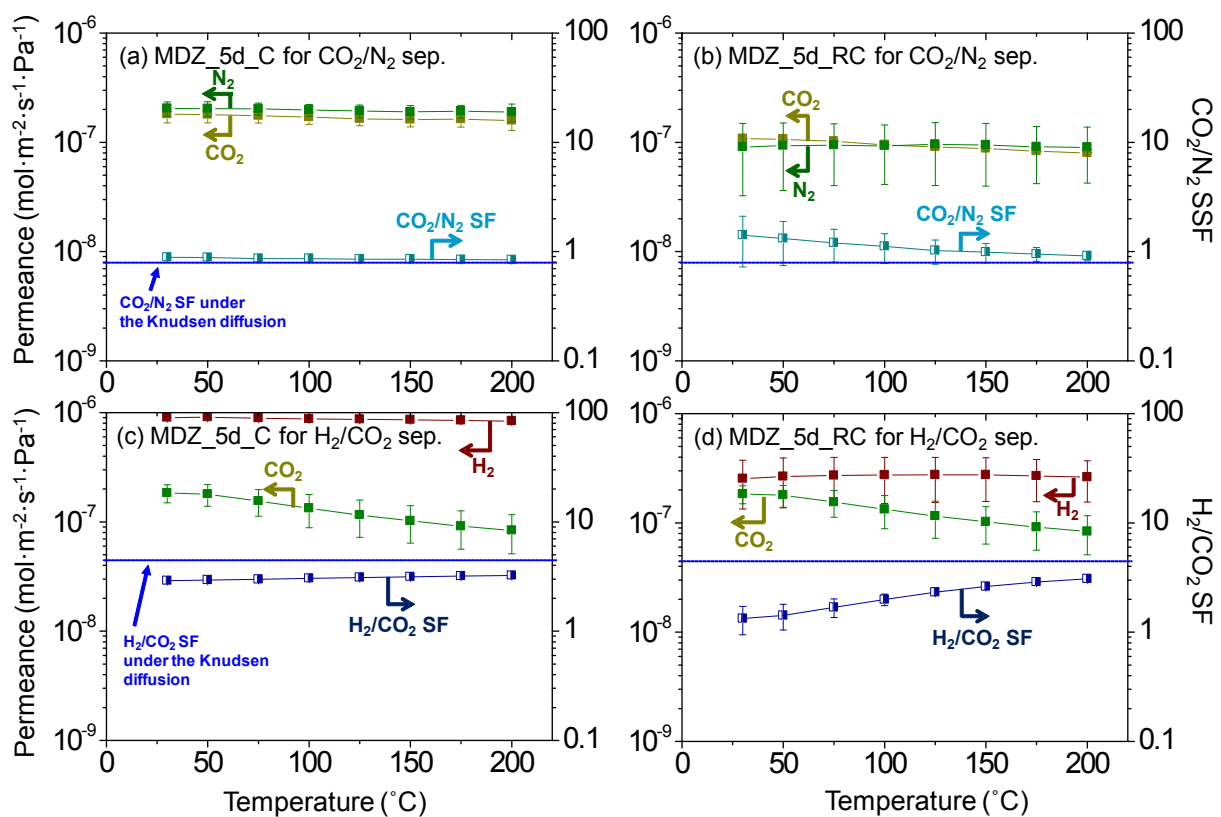
Fig. S8. Permeances of the binary mixtures of (a)-(b) CO_2/ N_2 and (c)-(d) H_2/CO_2 and the corresponding separation factors obtained through (a) & (c) MDZ_5d_C and (b) & (d) MDZ_5d_RC, respectively. For comparison, the CO_2/N_2 and H_2/CO_2 SFs, determined assuming Knudsen diffusion, are included as blue dashed lines.
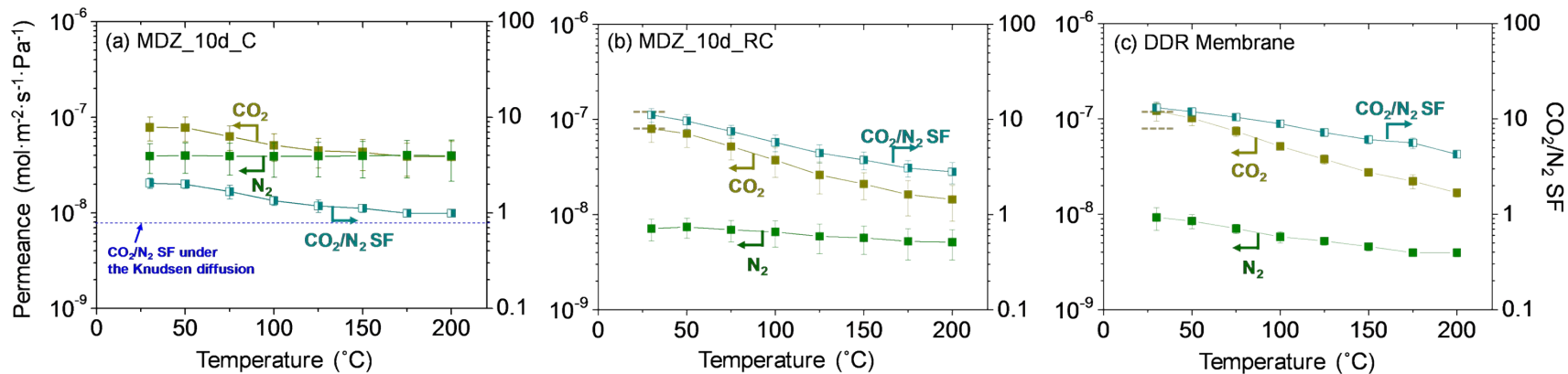
Fig. S9. Permeances of the equimolar binary mixtures of CO_2/N_2 and the corresponding SFs obtained through (a) MDZ_10d_C, (b) MDZ_10d_RC, and (c) DDR membrane[4] under dry conditions. In (a), the CO_2/N_2 SF, determined assuming Knudsen diffusion, is denoted by the blue dashed line. For better comparison, in (b)-(c), the CO_2 permeances at ca. 30 °C for MDZ_10d_RC and DDR membranes are indicated by the dark yellow dashed lines.
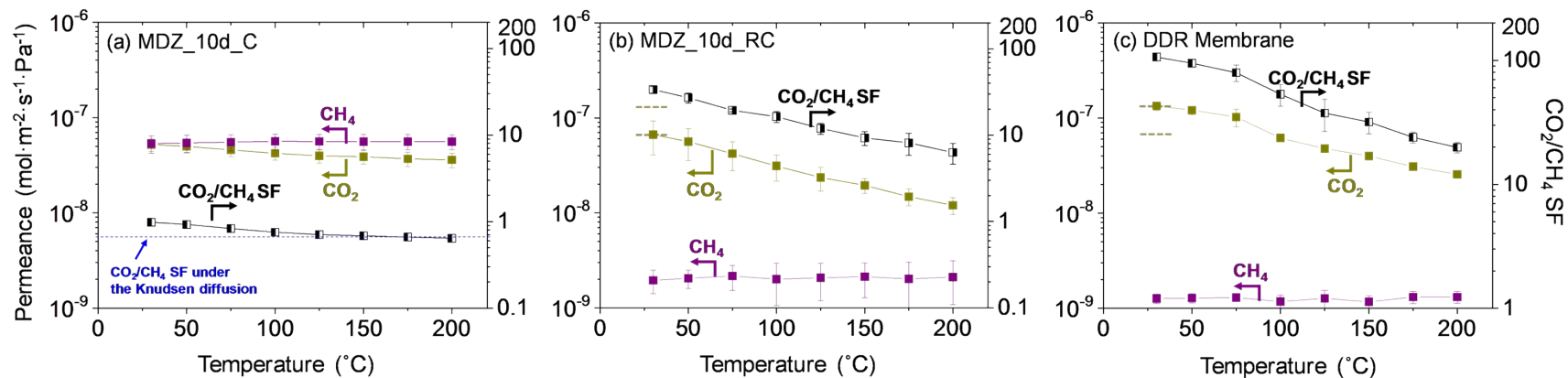
Fig. S10. Permeances of the equimolar binary mixtures of CO_2/CH_4 and the corresponding SFs obtained through (a) MDZ_10d_C, (b) MDZ_10d_RC, and (c) DDR membrane[4] under dry conditions. In (a), the CO_2/CH_4 SF, determined assuming Knudsen diffusion, is denoted by the blue dashed line. For better comparison, in (b)-(c), the CO_2 permeances at ca. 30 °C for MDZ_10d_RC and DDR membranes are indicated by the dark yellow dashed lines.
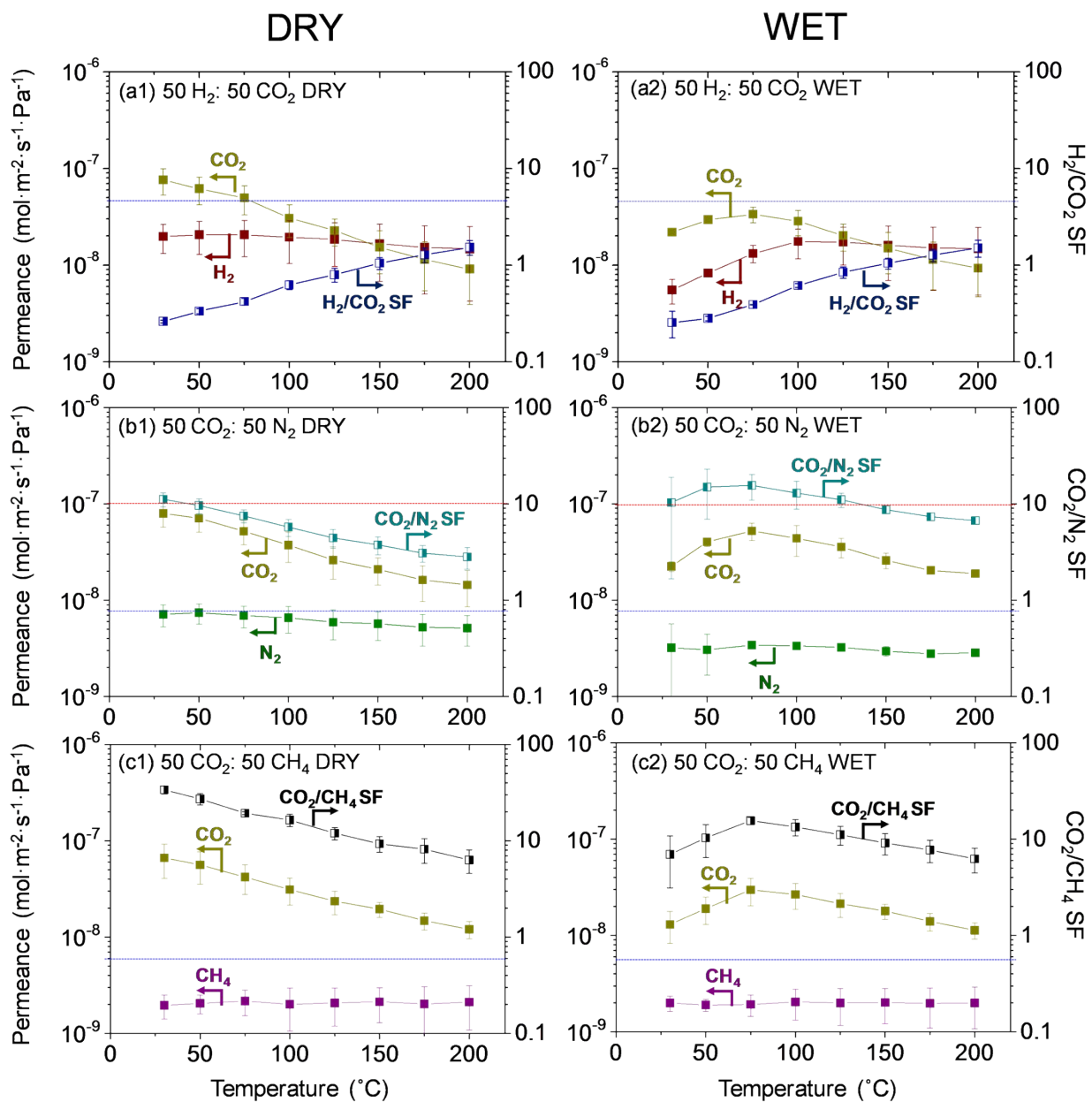
Fig. S11. Permeances of equimolar binary mixtures of (a1)-(a2) H_2/CO_2, (b1)-(b2) CO_2/N_2, and (c1)-(c2) CO_2/CH_4 and the corresponding SFs obtained through MDZ_10d_RC under dry (*left*) and wet (*right*) conditions. In all graphs, the H_2/CO_2, CO_2/N_2, and CO_2/CH_4 SFs, determined assuming Knudsen diffusion, are indicated by blue dashed lines. In addition, in (b2)-(b3), the CO_2/N_2 SF of 10 is included and indicated by the red dashed line.
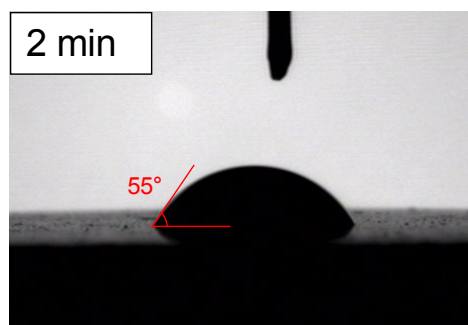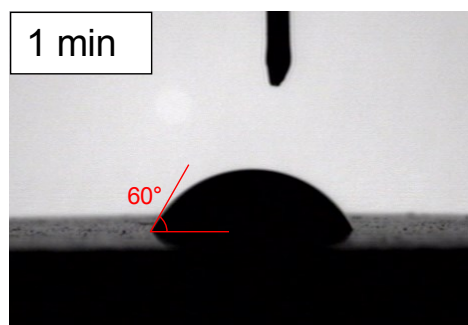
(a) MDZ_10d_C

0 s
20°

30 s

1 min

2 min

(b) MDZ_10d_RC

0 s
75°

1 min
60°

2 min
55°

5 min
52°
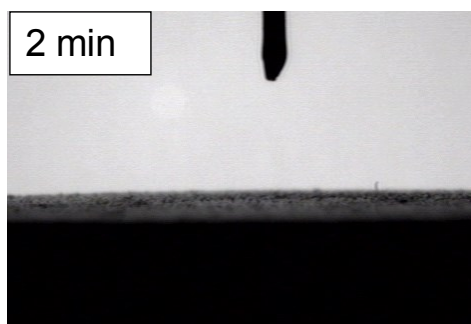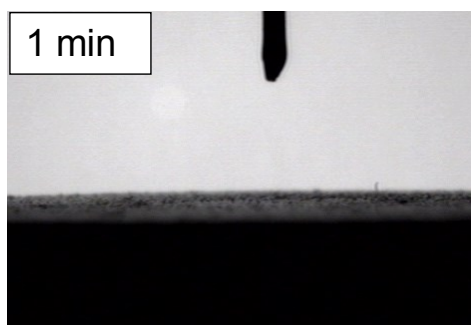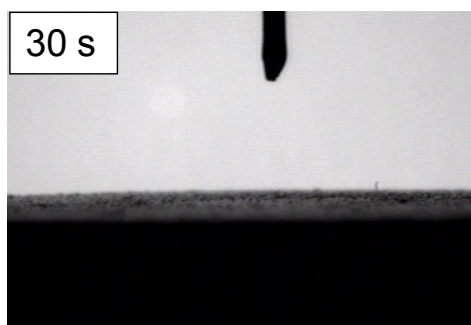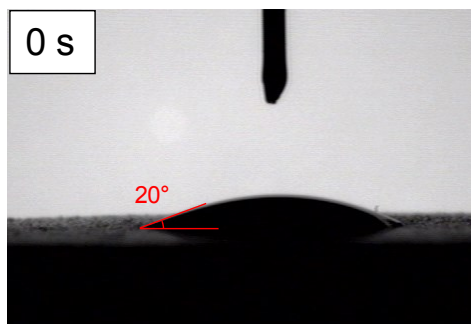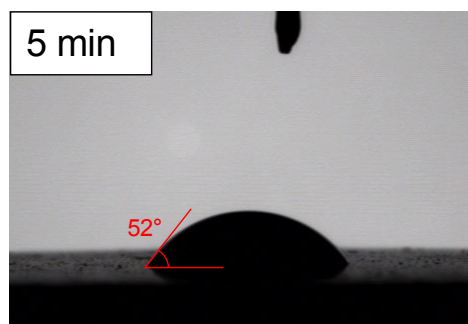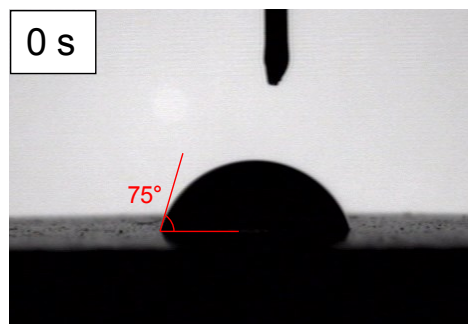
Fig. S12. Contact angles of water droplets on MDZ_10d_C (*left*) and MDZ_10d_RC (*right*) as a function of time.
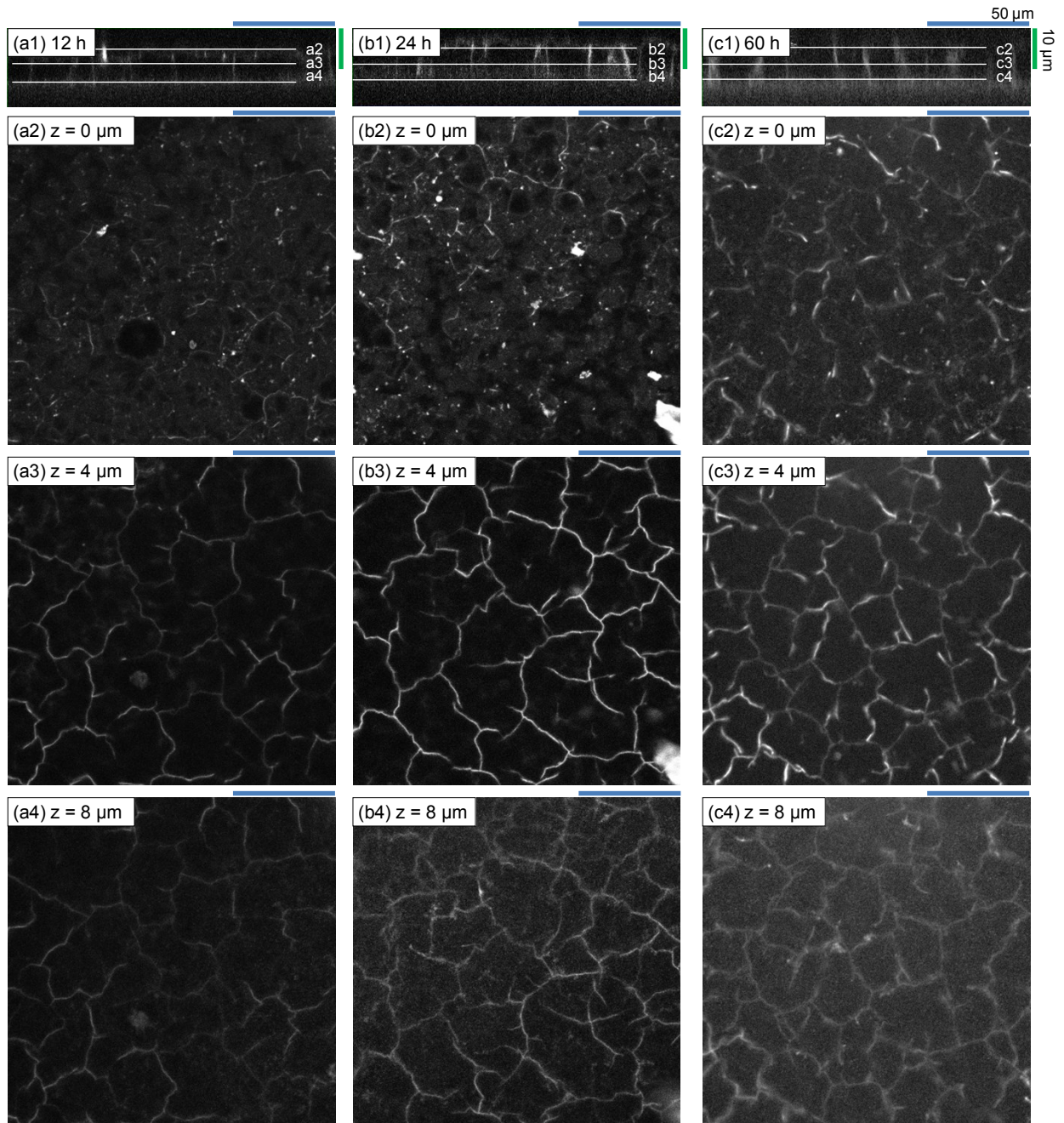
Fig. S13. (a1)-(c1) Cross-sectional view FCOM images of MDZ_10d_C along with (a2)-(c2), (a3)-(c3), and (a4)-(c4) top view FCOM images taken at the positions indicated in the cross-sectional view FCOM images after dyeing durations of 12 h, (a1)-(a4), 24 h, (b1)-(b4), and 60 h, (c1)-(c4). In the cross-sectional view, the blue (50 μm) and green (10 μm) bars represent the length scale in the horizontal and vertical directions, respectively, whereas the blue bars in the top view cover both horizontal and vertical directions.
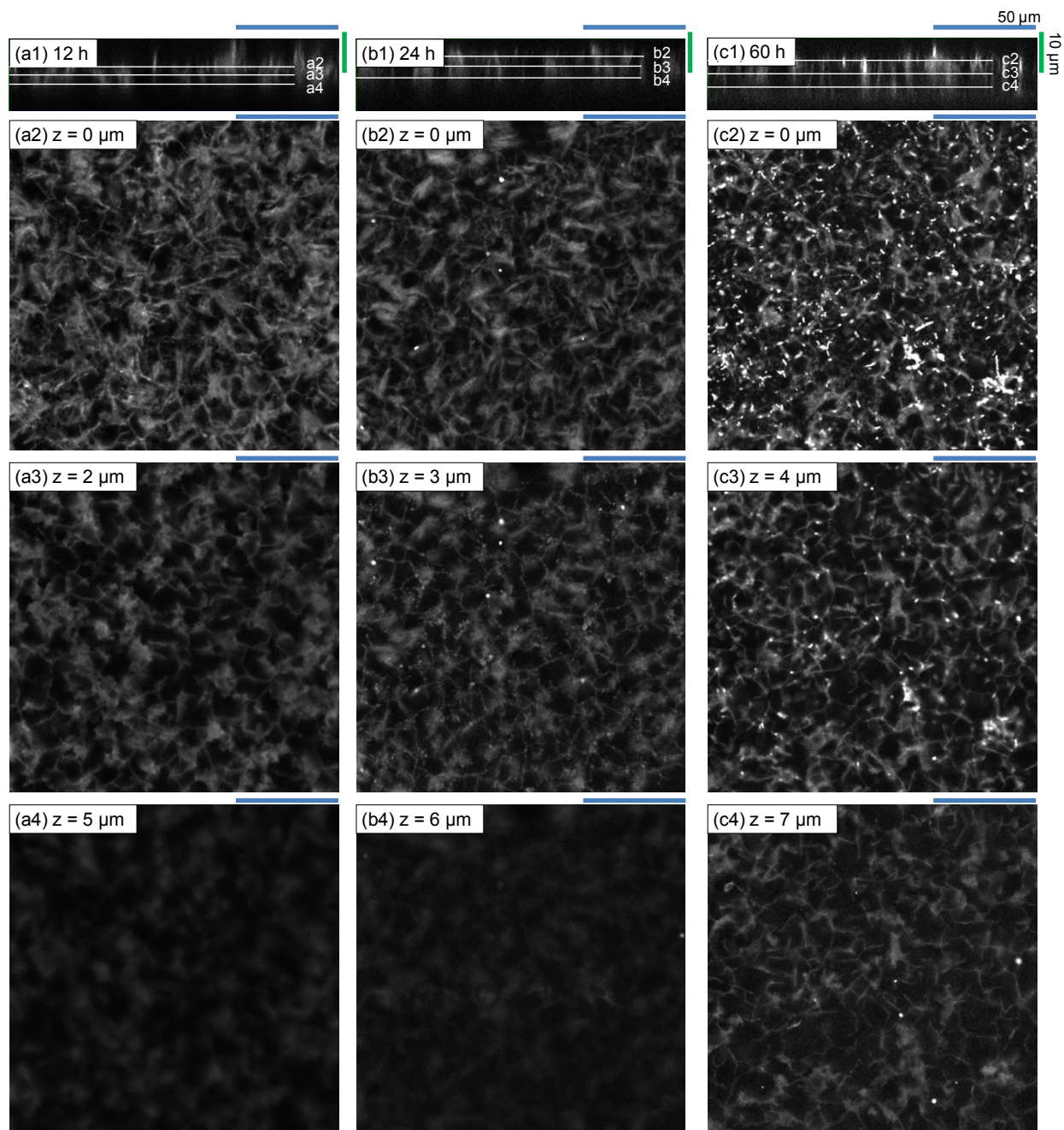
Fig. S14. (a1)-(c1) Cross-sectional view FCOM images of MDZ_10d_RC along with (a2)-(c2), (a3)-(c3), and (a4)-(c4) top view FCOM images taken at the positions indicated in the cross-sectional view FCOM images after dyeing durations of 12 h, (a1)-(a4), 24 h, (b1)-(b4), and 60 h, (c1)-(c4). In the cross-sectional view, the blue (50 μm) and green (10 μm) bars represent the length scale in the horizontal and vertical directions, respectively, while the blue bars in the top view cover both horizontal and vertical directions.

(a1)
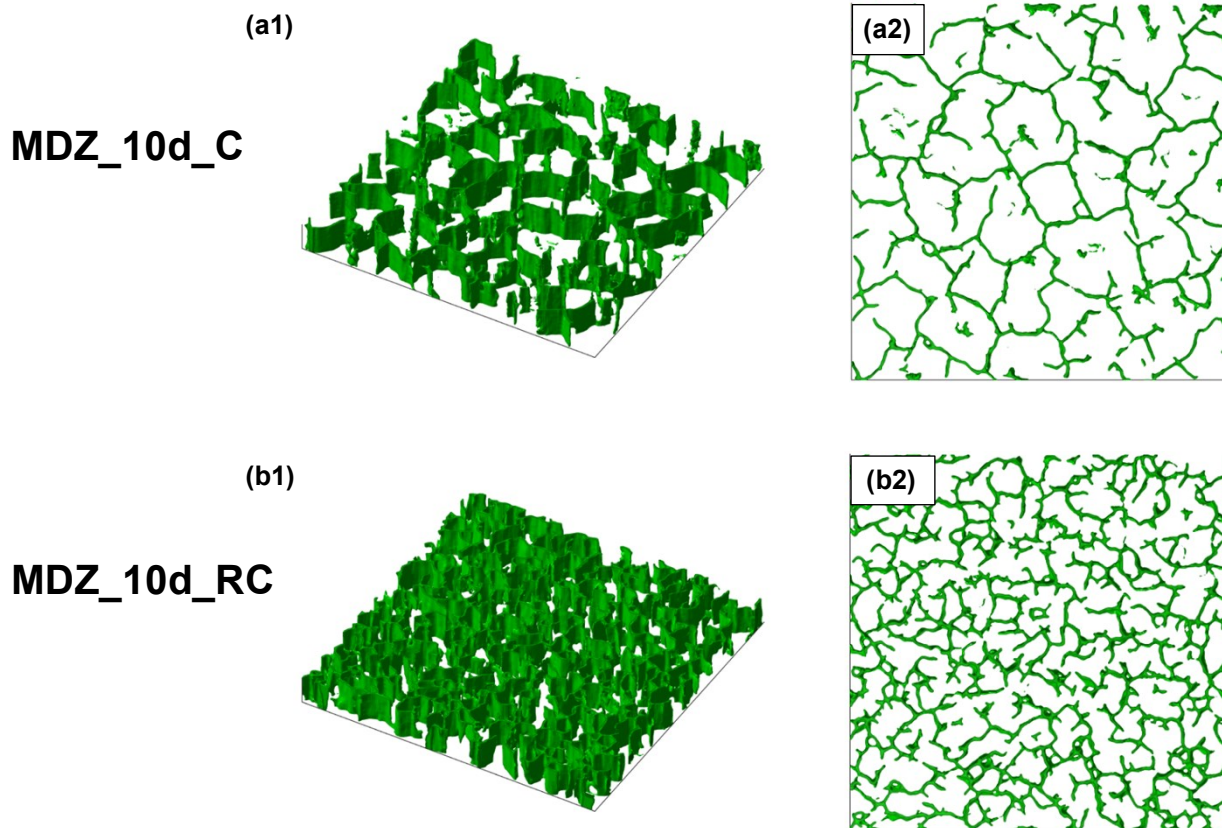
MDZ_10d_C

(b1)

MDZ_10d_RC

Fig. S15. Schematic illustration of the defect structures in (a1)-(a2) MDZ_10d_C and (b1)-(b2) MDZ_10d_RC, obtained via image analysis of the FCOM images shown in Figs. S13c1-c4 and S14c1-c4, respectively. Detailed information on the image analysis can be found elsewhere.[13]
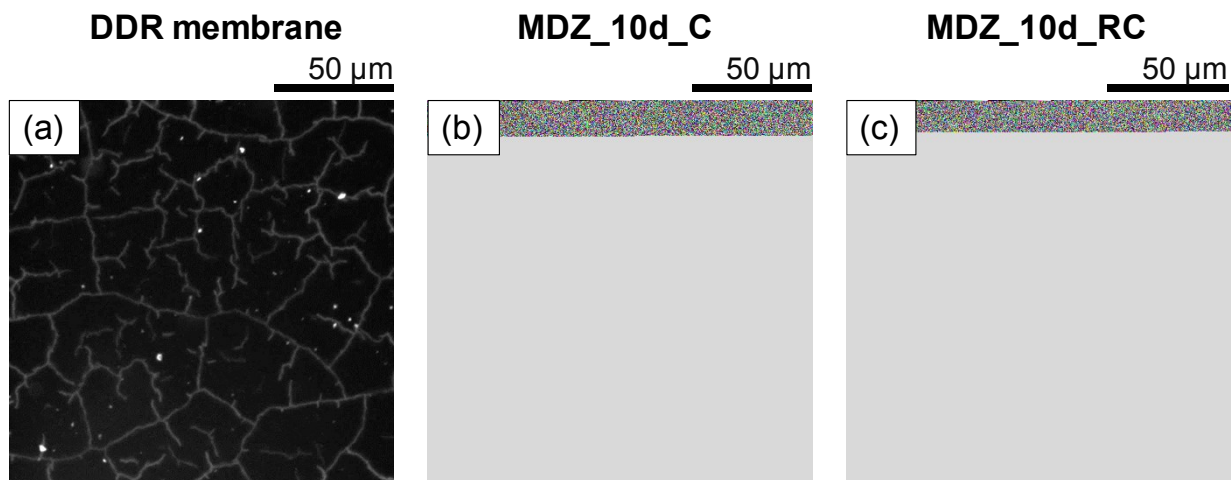
DDR membrane   **MDZ_10d_C**   **MDZ_10d_RC**

50 μm   50 μm   50 μm

Fig. S16. Top view FCOM images of (a) a homogeneous DDR membrane[4] along with those of (b) MDZ_10d_C and (c) MDZ_10d_RC. The images were taken approximately 4 μm below the membrane outer surface in each membrane.
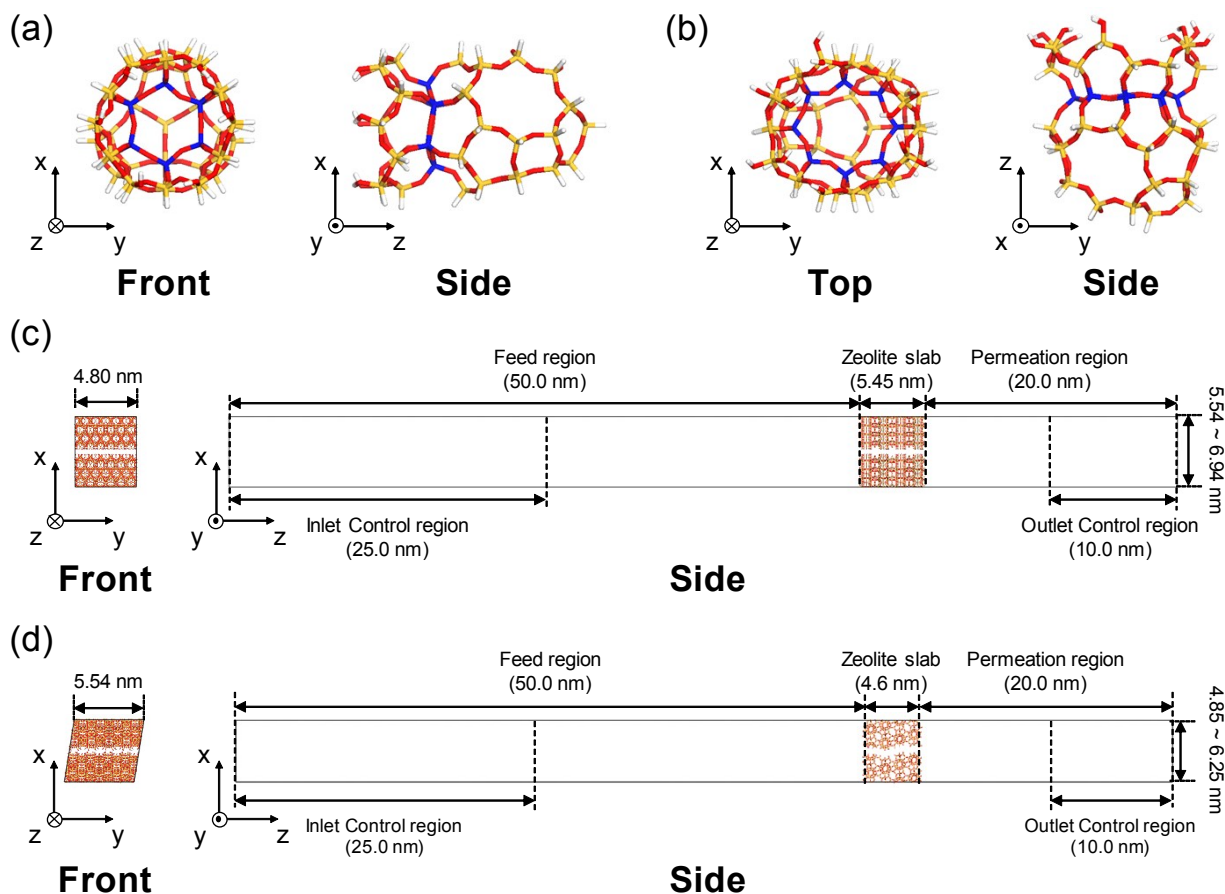
Fig. S17. (a)-(b) Cage-shaped cluster models of (a) DDR 46T and (b) 48T. (c) Slab model with the *z*-axis perpendicular to the (001) plane of the DDR zeolite. Depending on the width (*d*) of the planar defect, the height of the simulation box was changed from 5.54 (non-defective and *d* = 0.6 nm) to 6.94 nm (*d* = 2.0 nm). (d) Slab model with the *z*-axis perpendicular to the (101) plane of the DDR zeolite. Depending on the width (*d*) of the planar defect, the height of the simulation box was changed from 4.85 (non-defective and *d* = 0.6 nm) to 6.25 nm (*d* = 2.0 nm). In (a)-(b), silicon atoms that constitute 6- and 8-MR pore apertures, respectively, are marked in blue. Except these atoms, silicon, oxygen, and hydrogen atoms are marked in gold, red, and white, respectively.
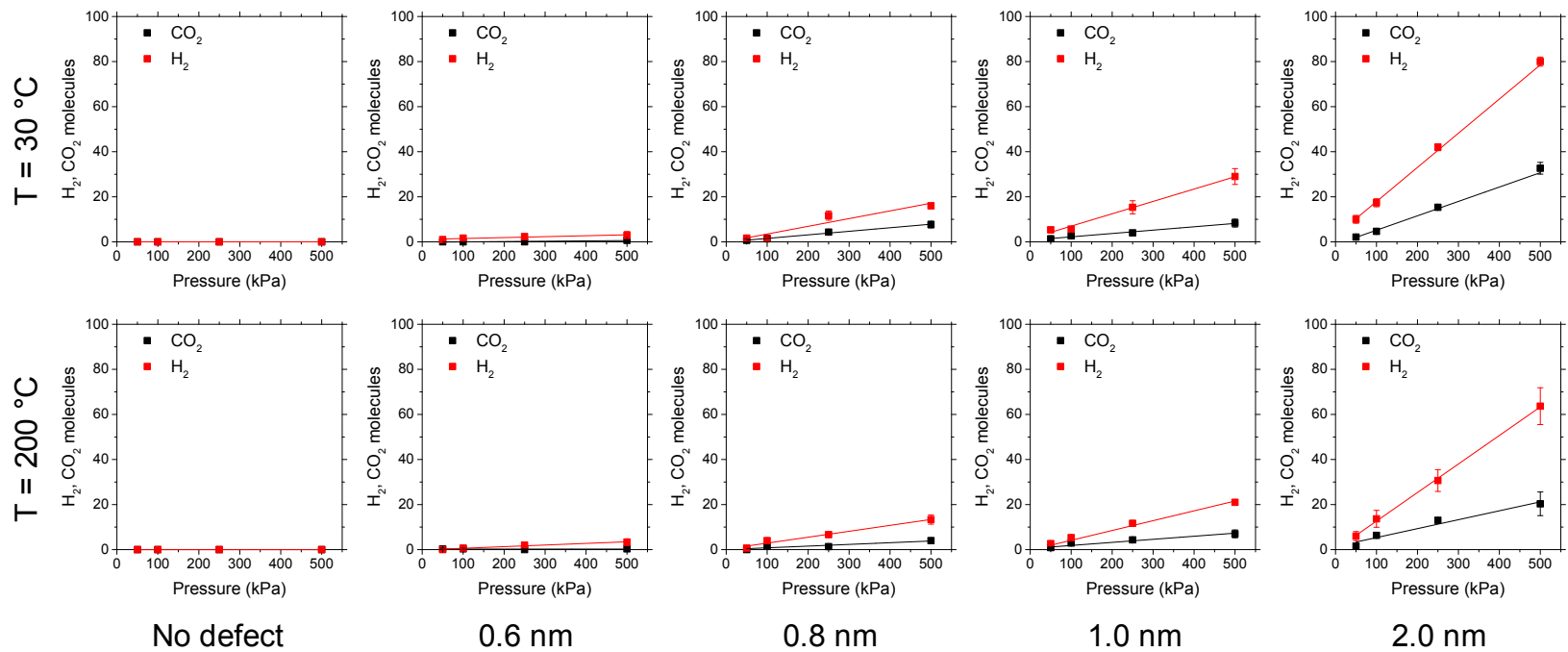
Fig. S18. Number of CO_2 and H_2 molecules passing through the *c*-oriented (i.e., *(001)*-out-of-plane oriented) DDR membrane at different total feed pressures, defect widths, and temperatures. The lines show the linear regression results.

Fig. S19. Number of CO_2 and H_2 molecules passing through the (*101*)-out-of-plane oriented DDR membrane at different total feed pressures, defect widths, and temperatures. The lines show the linear regression results.
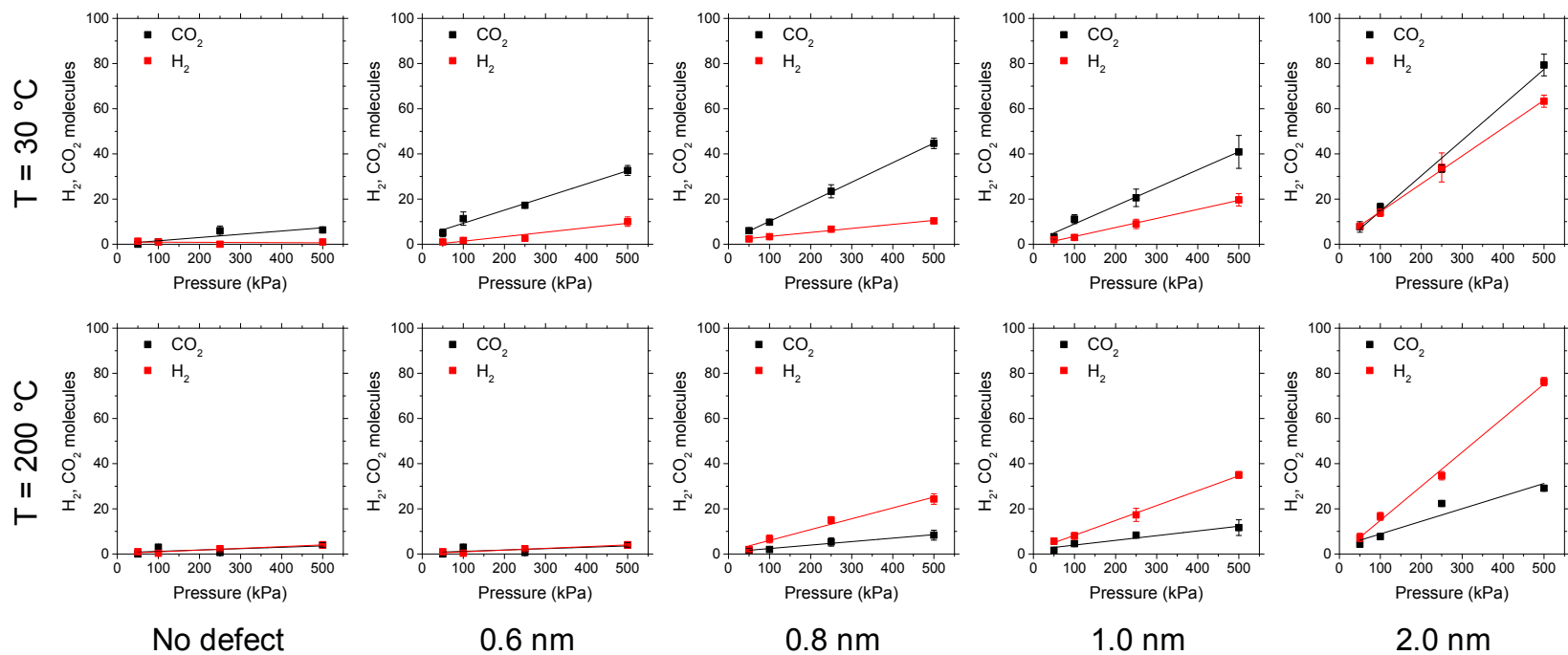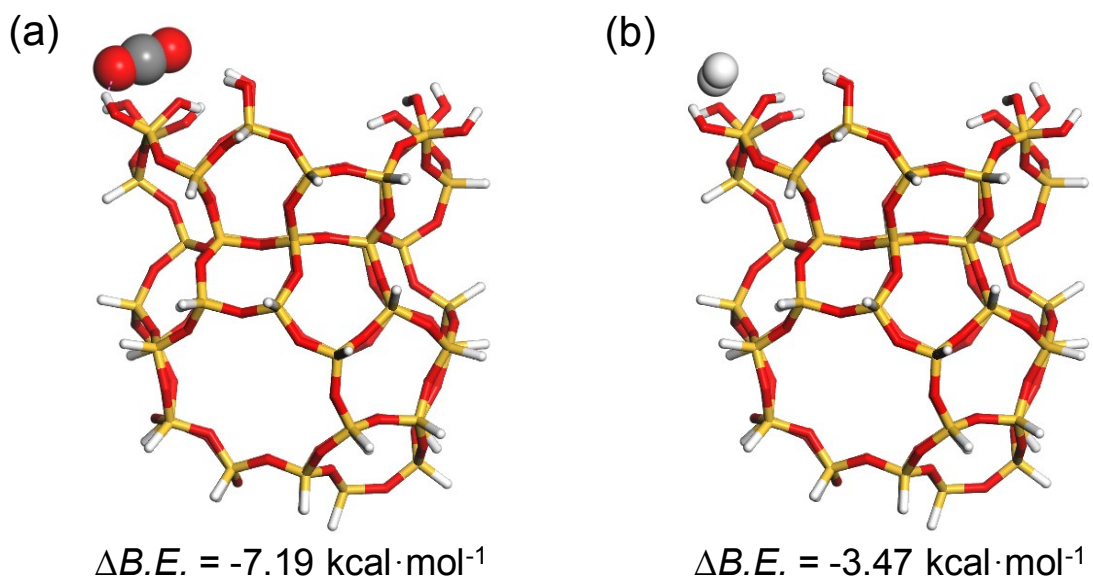
$\Delta B.E.$ = -7.19 kcal·mol^{-1} $\Delta B.E.$ = -3.47 kcal·mol^{-1}

Fig. S20. (a)-(b) DFT calculations of the adsorption of (a) CO_2 and (b) H_2 near the silanol groups of the DDR 48T model. The adsorbed gas molecule and the 48T model are shown in the CPK and stick models, respectively. In addition, silicon, oxygen, hydrogen, and carbon atoms are marked in gold, red, white, and gray, respectively.

(a)

$\Delta B.E.$ = -11.86 kcal·mol^{-1}

(b)

$\Delta B.E.$ = -4.25 kcal·mol^{-1}

Fig. S21. (a)-(b) DFT calculations of the adsorption of (a) CO_2 and (b) H_2 at the cage mouth of the 8-MR in the DDR 48T model. An adsorbed gas molecule and the 48T model are shown in the CPK and stick models, respectively. In addition, silicon, oxygen, hydrogen, and carbon atoms are marked in gold, red, white, and gray, respectively.
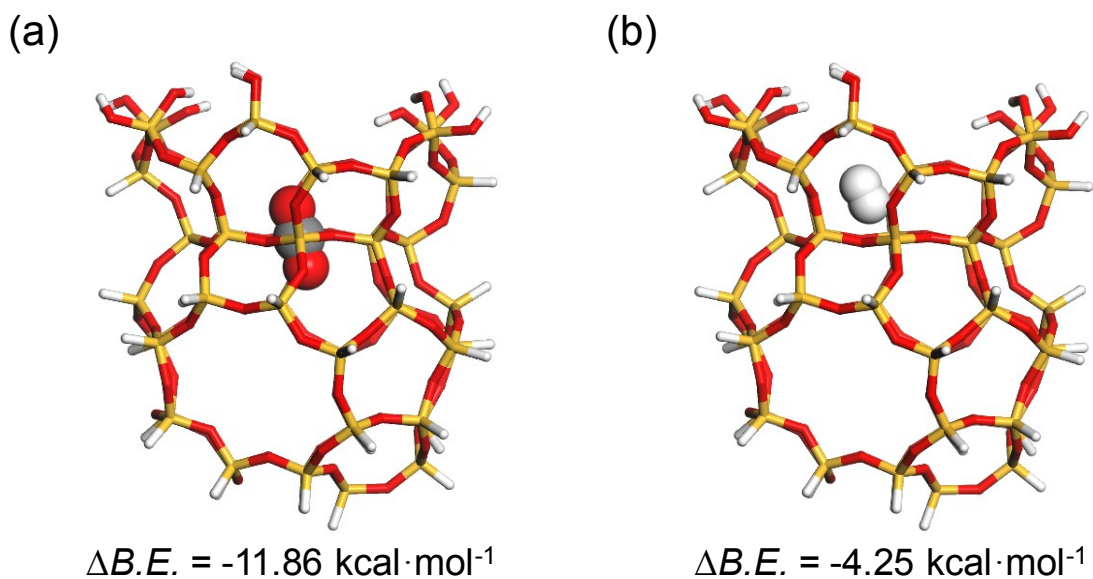
Table S1. Initial number of gas molecules in the feed region calculated by GCMC simulation.

Temperature		Initial number of gas molecules in the feed region used for molecular dynamics							
		30 °C				200 °C			
Defect (nm)	Partial pressure (kPa)	(*001*)-oriented		(*101*)-oriented		(*001*)-oriented		(*101*)-oriented	
		CO_2	H_2	CO_2	H_2	CO_2	H_2	CO_2	H_2
Non-defect (0.0) & 0.6	50	16	16	16	16	10	10	10	10
	100	32	32	32	32	20	20	21	21
	250	81	79	82	80	51	51	52	51
	500	166	158	167	160	102	101	104	102
0.8	50	17	16	17	17	11	11	11	11
	100	33	33	34	33	21	21	21	21
	250	84	82	85	83	53	53	54	53
	500	172	164	174	166	106	105	108	106
1.0	50	17	17	17	17	11	11	11	11
	100	34	34	35	35	22	22	22	22
	250	87	85	89	87	55	54	56	55
	500	178	170	181	173	109	109	112	111
2.0	50	20	20	21	21	13	13	13	13
	100	40	40	42	41	26	26	27	26
	250	101	99	105	103	64	64	66	66
	500	207	198	215	205	128	127	133	132

References

1. A. Corma, V. Fornes, S.B. Pergher, T.L.M. Maesen and J.G. Buglass, *Nature*, 1998. **396**(6709), 353-356.
2. E. Kim, W. Cai, H. Baik and J. Choi, *Angew. Chem., Int. Ed.*, 2013. **52**(20), 5280-5284.
3. T. Tomita, K. Nakayama and H. Sakai, *Microporous Mesoporous Mater.*, 2004. **68**(1-3), 71-75.
4. E. Kim, S. Hong, E. Jang, J.H. Lee, J.C. Kim, N. Choi, C.H. Cho, J. Nam, S.K. Kwak, A.C.K. Yip and J. Choi, *J. Mater. Chem. A*, 2017. **5**(22), 11246-11254.
5. J. Choi, S. Ghosh, Z.P. Lai and M. Tsapatsis, *Angew. Chem., Int. Ed.* , 2006. **45**(7), 1154-1158.
6. J. Kim, E. Jang, S. Hong, D. Kim, E. Kim, H. Ricther, A. Simon, N. Choi, D. Korelskiy, S. Fouladvand, J. Nam and J. Choi, *J. Membr. Sci.*, 2019. **591**, 10.
7. A. Boultif and D. Louër, *J. Appl. Cryst.*, 2004. **37**(5), 724-731.
8. J. Rodríguez-Carvajal, *Physica B*, 1993. **192**(1-2), 55-69.
9. A. Le Bail, *Powder Diffr.*, 2005. **20**(4), 316-326.
10. V. Petříček, M. Dušek and L. Palatinus, *Z. Kristallogr.*, 2014. **229**(5), 345-352.
11. J. Choi, H.K. Jeong, M.A. Snyder, J.A. Stoeger, R.I. Masel and M. Tsapatsis, *Science*, 2009. **325**(5940), 590-593.
12. T. Lee, J. Choi and M. Tsapatsis, *J. Membr. Sci.*, 2013. **436**, 79-89.
13. S. Hong, D. Kim, Y. Jeong, E. Kim, J.C. Jung, N. Choi, J. Nam, A.C.K. Yip and J. Choi, *Chem. Mater.*, 2018. **30**(10), 3346-3358.
14. G. Barone, N. Armata, A. Prestianni, T. Rubino, D. Duca and D.Y. Murzin, *J. Chem. Theory Comput.*, 2009. **5**(5), 1274-1283.
15. V. Shapovalov and A.T. Bell, *J. Phys. Chem. C*, 2010. **114**(41), 17753-17760.
16. B. Delley, *J. Chem. Phys.*, 1990. **92**(1), 508-517.
17. B. Delley, *J. Chem. Phys.*, 2000. **113**(18), 7756-7764.
18. J.P. Perdew, K. Burke and M. Ernzerhof, *Phys. Rev. Lett.*, 1996. **77**(18), 3865-3868.
19. A. Tkatchenko and M. Scheffler, *Phys. Rev. Lett.*, 2009. **102**(7), 073005.
20. S. Plimpton, *J. Comput. Phys.*, 1995. **117**(1), 1-19.
21. J.G. Harris and K.H. Yung, *J. Phys. Chem.*, 1995. **99**(31), 12021-12024.
22. A.V.A. Kumar, H. Jobic and S.K. Bhatia, *J. Phys. Chem. B*, 2006. **110**(33), 16666-16671.
23. R.T. Cygan, J.J. Liang and A.G. Kalinichev, *J. Phys. Chem. B*, 2004. **108**(4), 1255-1266.
24. Dassault Systèmes BIOVIA, Materials Studio 2018, San Diego: Dassault Systèmes, 2018.
25. Y. Jeong, S. Hong, E. Jang, E. Kim, H. Baik, N. Choi, A.C.K. Yip and J. Choi, *Angew. Chem., Int. Ed.*, 2019. **58**(51), 18654-18662.